Advanced Quantum Technologies

Quantum computation with electrons trapped on liquid Helium by manipulating their lateral orbital states

--Manuscript Draft--

Manuscript Number:	qute.202300307
Article Type:	Research Article
Corresponding Author:	Lianfu Wei Southwest Jiaotong University School of Information Science and Technology Chengdu, CHINA
Order of Authors:	Yufen Li, Ph.D.
	Suirong He
	Miao Zhang
	Lianfu Wei
Keywords:	electrons on liquid Helium; lateral orbital states; qubits; addressable manipulations; quantum computation
Abstract:	Surface-state electrons floating on liquid Helium have served as one of the great potential experimental platforms to implement quantum computation, as the qubits can be encoded by the lowest two levels of their vertical vibrations (i.e., Hydrogen-like atoms), lateral vibrations, and electronic spins. Given the qubit encoded by the lateral vibration of a trapped electron and its interaction with the transmission line resonator have been demonstrated experimentally, here we investigate how to implement the single- and two-qubit gates with a designed trapped-electron array by manipulating the lateral-vibration states of the trapped electrons. It is shown that, by biasing the electrodes and driving the coplanar waveguide transmission line resonator, at the bottom of liquid Helium, the electrons can be individually trapped on a series of anharmonic potentials, generating a Paul-like trap array, on liquid Helium. The eigenfrequencies of the qubits and the interbit interactions are experimentally manipulated and thus the desired single-qubit operations on the individually addressable trapped electrons, switchable two-qubit manipulations between the electrons trapped in the distant traps, and also the high-fidelity readouts of qubits can be implemented by applying the circuit quantum electrodynamics techniques. The feasibility of the proposal is discussed, in detail, through the numerical simulations.

Quantum computation with electrons trapped on liquid Helium by manipulating their lateral orbital states

Yufen Li[1], **Suirong He**[1], **Miao Zhang**[2] **and Lianfu Wei**[1*]

[1] Information Quantum Technology Laboratory, International Cooperation Research Center of China Communication and Sensor Networks for Modern Transportation, School of Information Science and Technology, Southwest Jiaotong University, Chengdu 610031, China

[2] School of Physical Science and Technology, Southwest Jiaotong University, Chengdu 610031, China

[*] Author to whom any correspondence should be addressed.

E-mail: yfli@my.swjtu.edu.cn; hesuirong@163.com; zhangmiao@swjtu.edu.cn; lfwei@swjtu.edu.cn

Abstract. Surface-state electrons floating on liquid Helium have served as one of the great potential experimental platforms to implement quantum computation, as the qubits can be encoded by the lowest two levels of their vertical vibrations (i.e., Hydrogen-like atoms), lateral vibrations, and electronic spins. Given the qubit encoded by the lateral vibration of a trapped electron and its interaction with the transmission line resonator have been demonstrated experimentally, here we investigate how to implement the single- and two-qubit gates with a designed trapped-electron array by manipulating the lateral-vibration states of the trapped electrons. It is shown that, by biasing the electrodes and driving the coplanar waveguide transmission line resonator, at the bottom of liquid Helium, the electrons can be individually trapped on a series of anharmonic potentials, generating a Paul-like trap array, on liquid Helium. The eigenfrequencies of the qubits and the interbit interactions are experimentally manipulated and thus the desired single-qubit operations on the individually addressable trapped electrons, switchable two-qubit manipulations between the electrons trapped in the distant traps, and also the high-fidelity readouts of qubits can be implemented by applying the circuit quantum electrodynamics techniques. The feasibility of the proposal is discussed, in detail, through the numerical simulations.

Keywords: electrons on liquid Helium, lateral orbital states, qubits, addressable manipulations, quantum computation

1. Introduction

The researches of practical quantum computation have been paid much attention in recent years [1]. In 2019, the so-called “quantum supremacy” has first been demonstrated with 53-bit programmable superconducting qubits, and thus using the quantum processors to exponential speedup over its classical counterpart is desirably feasible [2]. In addition, a

series of experimentally quantum information processors, typically, e.g., the linear optical Bose sampler [3], superconducting adiabatic quantum quenching [4], and the optical coherent Ising machines [5, 6], etc., have also demonstrated the realistic possibility of the quantum computation. Indeed, a series of physical systems typically such as the superconducting Josephson junction circuits [7], trapped ions [8–14], linear optical quantum systems [15, 16], and also the semiconductor quantum dot arrays [17–19], etc., have been demonstrated to implement the desired quantum computation.

In comparison, although the Hydrogen-like atomic states [20], lateral orbital states [21], and spin states [22] of electrons trapped on liquid Helium have been demonstrated to encode the qubits for the implementation of quantum computation, the desired universal quantum gates with such a system have been paid relatively little attention, probably due to certain realistic difficulties. First, the relevant device is relatively difficult to be generated, as floating the electrons on liquid Helium is not easily realized experimentally. Second, the millimeter wave (MMW) pulse technique (rather than the usual centimeter wave (CMW) one widely applied in the circuit quantum electrodynamics (QED) system) is required to implement the manipulations of the qubits encoded by the lowest two levels of the Hydrogen-like atom [20]. However, given such a physical system possesses certain unique advantages, typically such as the particularly pure environment with significantly less noise [22, 23] and the relatively easy to be scalable by conveniently setting the electrodes at the bottom of Helium to generate the qubit array [24], quantum computation with the electrons trapped on liquid Helium is still desirable. In fact, benefited from the significantly long coherent times of the Hydrogen-like atomic states and the electric spin states, various coherent quantum manipulations have been proved theoretically, e.g., the realization of Jaynes-Cummings model [25, 26], image charge detection of Rydberg state [27, 28], spin state controls [21], and possible MMW photonic crystal with adjustable band gap [29], etc. have been proposed. Noted that most of these manipulations are on the vertical-state qubits, generated by vibration of the electron along the direction which is perpendicular to the liquid Helium surface, and the MMW-pulse technique [30], instead of the well-developed CMW one, is required to be developed particularly.

Interestingly, in a recent work Schuster et al. [24] demonstrated that, besides the vibrational trap of the electrons along the perpendicular direction, the lateral motion of the electrons on liquid Helium can also be trapped by applying properly-biased electrodes at the bottom of liquid Helium. Given the transition frequency between the lowest two levels of these orbital quantum states is in the usual CMW band and thus the corresponding qubits can be manipulated by using the circuit QED technique. Specifically, the lateral motions of one, two, three, and four electrons in a trap and their interactions with the quantized transmission line resonator had been successfully demonstrated [24]. Inspired by such a pioneer work, in this paper, we discuss the feasibility of using the lateral nonharmonic motion (rather than the vertical Hydrogen-like atoms) of the trapped electrons to implement quantum computation. We first discuss how the electrons can be individually trapped on a series of anharmonic potentials, generating a Paul-like trap array [13], on liquid Helium, by designing the proper biases of the electrodes and the coplanar waveguide transmission line resonator (CPW-TLR)

at the bottom of liquid Helium. Next, we investigate the robustness of the qubits encoded by the lowest two levels of the nonlinear lateral vibration (rather than the vertical ones) and the feasibility of the desired addressable manipulations for quantum computation with such a scalable qubit array.

The paper is organized as follows: In Section 2, we design a generic one-dimensional potential array to confine the electrons in a series of traps on liquid Helium. We show that the lowest two levels of the lateral anharmonic vibration of the electron in each trap can be utilized to encode the qubit, whose eigenfrequency is in the CMW band. In Section 3, by making use of a driven CPW-TLR at the bottom of liquid Helium as the date bus, we demonstrate how to implement the individually addressable single-qubit operations of the arbitrarily selected single qubits, and the two-qubit logic gate operations between two arbitrarily selected distant qubits. The quantum non-demolition (QND) readout(s) of the qubit(s) in both frequency- and time domains are simulated numerically in Section 4. We show also here that, the pure- and mixed states of the qubits could be distinguished effectively. Finally, the conclusion is given in Section 5.

2. The robustness of the qubit encoded by the lateral anharmonic vibration of the electron trapped on liquid Helium

Let us consider a planar chip schematically shown in Figure 1, wherein a series of electrons are trapped one by one, generating a trapped-electron array on liquid Helium. Floating electrons

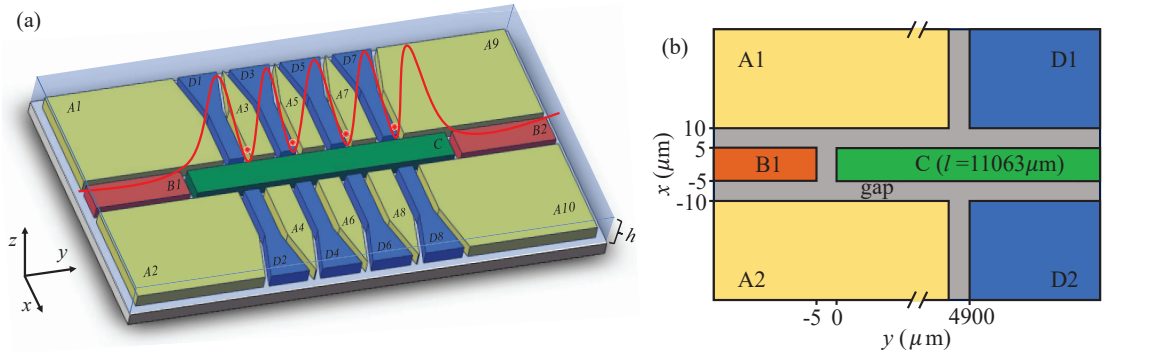

Figure 1. A trapped-electron array on liquid Helium generated by the DC-bias electrodes and an rf-driving CPW-TLR. (a) The designed chip, wherein A1-A10 are the grounds, B1 and B2 are the CPW feed lines separated by a CPW-TLR (C), and D1-D8 are the DC-biased electrodes used to confine the x-direction motions of the trapped electrons, and the surface of the chip is coved by a layer of liquid Helium with the thickness $h \sim 500$ nm [31]. A standing wave is excited and a series of potentials are generated to trap a series of electrons and drive the y-direction anharmonic vibrations of the trapped electrons. (b) The designed parameters of an unit of the chip, which will be utilized to the following numerical simulations. Here, the unit size is 12000 μm×100 μm, the thickness of the sapphire substrate is set as 400 μm, the widths of the TLR and the gaps are set as 10 μm and 5 μm, respectively.

on liquid Helium had been demonstrated experimentally many years ago (see, e.g., [30]), as Helium is a noble gas that can be liquidated at a temperature below about 4.125 K. According to the Pauli exclusion principle, a potential barrier (about 1 eV [32]) prevents

the electron from the liquid Helium. As a consequence, the electron can be floated on liquid Helium and its motion along the vertical direction generates a Hydrogen-like atom. In fact, electrons floating on liquid Helium have also served as one of the promising platforms to investigate various physical behaviors of two-dimensional electron gas [33, 34] and Wigner crystal [29, 35]. Experimentally, various interesting physical effects of the electrons trapped on liquid Helium have been widely investigated [31, 36]. Alternatively, to implement the desired quantum computation in CMW band, in the present work, we focus on the quantum manipulations of a series of single electrons trapped on liquid Helium. For the manipulability, the potentials for trapping the electrons can be generated by the voltage-biased electrodes at the bottom of liquid Helium and driven by coupling with the CPW-TLR. Typically, the vibrations of the electrons can be confined only along the lateral y-direction [24], and the CPW-TLR, located also at the bottom of liquid Helium, plays double roles. First, it is utilized to generate a series of rf standing wave potentials to trap the electrons [37–39], assisted by the static electric fields generated by the electrodes. Secondly, its quantized fundamental mode can be served as the data bus to implement the desired qubit manipulations [24, 41, 42].

2.1. Quantization of the lateral vibrations of the trapped electrons on liquid Helium

Without loss of generality, we first discuss a single electron trapped on liquid Helium. The potential of a trapped electron can be written as [20, 31]:

$$U(x,y,z) = -\frac{\Lambda e^2}{4\pi\varepsilon_0 z} + eE(t)\sqrt{(h+z)^2+x^2+y^2}, \tag{1}$$

where e is the electronic charge, h represents the thickness of liquid Helium, z is the vertical vibration of the trapped electron along the z-direction. Like the Paul trap to trap the ions [13], here $E(t)$ is the strength of the total electric field, which is the superposition of the strong static one E_{dc} (generated by the biases of the electrodes) and the relatively weak rf standing wave one $E_{rf}(t)$ (which is excited by driving the CPW-TLR [37–39]). Also, $\Lambda = (\varepsilon-1)/[4(\varepsilon+1)]$ with $\varepsilon = 1.05723$ and $\varepsilon_0 = 8.8541878128\times10^{-12}$ F/m are the relative permittivity of liquid Helium and the vacuum dielectric constant, respectively. As $x, y, z \ll h$, the above potential can be effectively approximated as (See Appendix A)

$$U \approx -\frac{\Lambda e^2}{4\pi\varepsilon_0 z} + \frac{eE(t)\left(8h^4+8h^3z+4h^2x^2-x^4+4h^2y^2-y^4\right)}{8h^3}. \tag{2}$$

Therefore, the Hamiltonian of the electronic states can be written as

$$\hat{H}_a = \hat{H}_z + \hat{H}_x + \hat{H}_y, \tag{3}$$

where

$$\hat{H}_z \approx \frac{\hat{p}_z^2}{2m} - \frac{\Lambda e^2}{4\pi\varepsilon_0 z} + eE_{dc}z, \tag{4}$$

describes a Hydrogen-like atomic motion of the trapped electron along the direction perpendicular to the liquid surface, with m being the mass of the electron and $\hat{p}_z$ the

momentum operator. The vertical motion can be neglected for the manipulations of the lateral motion, as the transition frequency (which is in the MMW band) between the lowest two energy levels of such a Hydrogen-like atom is much higher than the vibrational frequency (in the CMW band) of the trapped electron along the y-direction parallel to liquid Helium surface. Furthermore, with the configuration shown in Fig. 1 the vibrations of the trapped electrons along the x-direction are strongly limited and thus these motions can be ignored. As a consequence, only the vibration along the y-direction, i.e., the axial one of the resonator, of the trapped electron is considered, and thus the Hamiltonian in Eq. (3) reduces to

$$\hat{H}_a \approx \frac{\hat{p}_y^2}{2m} + U_y,\ U_y = \frac{eE_{dc}}{2h}y^2 - \frac{eE(t)}{8h^3}y^4. \tag{5}$$

Obviously, it describes a one-dimensional nonlinear vibration; a linear harmonic oscillator $\hat{H} = \hat{p}^2/(2m) + m\omega_y^2 y^2/2$ with a vibrational frequency [31]: $\omega_y = \sqrt{eE(t)/(mh)}$, pluses a nonlinear perturbation term $\sim y^4$. In the representation of the number of linear vibrational phonons, the Hamiltonian (5) can be expressed as:

$$\hat{H}'_a = \hbar\omega_y\left(\hat{a}^\dagger\hat{a} + \frac{1}{2}\right) - \frac{\hbar^2}{32mh^2}(\hat{a} + \hat{a}^\dagger)^4. \tag{6}$$

Here, $\hbar$ is Planck constant, $\hat{a}$ ($\hat{a}^\dagger$) is the Bosonic annihilation (creation) operator of the vibrational phonon and $[\hat{a}, \hat{a}^\dagger] = 1$. Under the first-order approximation, the eigenvalue of

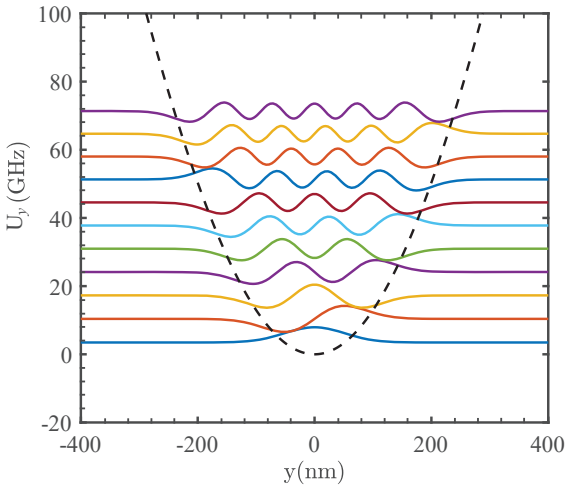

Figure 2. The potential and the stationary wave functions of the trapped electron. The black dotted line represents the trapped-electron potential, and the bottom blue and red curves are the stationary wave functions of the electron being trapped in the energy ground state and the first excited one, respectively. The relevant parameters are set as: h = 500 nm and E_{dc} = 53.87 V/cm.

the Hamiltonian (5) can be easily obtained as

$$E_n = \langle n|\hat{H}'_a|n\rangle \approx \hbar\omega_y\left(n + \frac{1}{2}\right) - \frac{3\hbar^2(2n^2 + 2n + 1)}{32mh^2}, \tag{7}$$

for the eigenstate $|n\rangle$, $n = 0, 1, 2, 3, \ldots$. Fig. 2 shows the y-dependent potential of the nonlinear vibration and the corresponding stationary wave functions of the trapped electron. Specifically, if the thickness of liquid Helium and the strength of the electrostatic field are respectively set typically as $h = 500$ nm and $E_{dc} = 53.87$ V/cm, then the frequency of the linear vibration of the electron along the y-direction is calculated as $f_y = \omega_y/(2\pi) = \sqrt{eE_{dc}/(mh)}/(2\pi) \approx 6.9282$ GHz, which is much lower than the frequency of the Hydrogen-like atomic vibration along the direction perpendicular to the liquid Helium surface. Therefore, the vertical z-direction vibration is safely decoupled from that of the lateral y-direction. The energy of the vibrational ground state and the first excited one of such a nonlinear harmonic oscillator are respectively calculated as: $E_0 = \hbar\omega_y/2 - 3\hbar^2/(32mh^2) \approx 14.296$ μeV, and $E_1 = 3\hbar\omega_y/2 - 15\hbar^2/(32mh^2) \approx 42.832$ μeV, with the transition frequency between them being: $\omega_a = (E_1 - E_0)/\hbar \approx 2\pi \times 6.9$ GHz, which is closed the experimental observation [24, 40].

The above calculation indicates that, the lowest two energy stationary states: $|0\rangle$ and $|1\rangle$, of this nonlinear harmonic oscillator, can be utilized to encode the desired qubit, whose eigenfrequency is really in the CMW band. Compared with the MMW band microwave pulses required to implement the quantum manipulations of the Hydrogen-like atomic qubits [20], the technique by using the microwave pulses in MMW band to manipulate the present qubit is developed well and has been widely applied in the current solid-state circuit QED systems [38].

2.2. Qubit level stability

In this subsection, we confirm that the proposed qubit encoded by the two lowest levels of the anharmonic oscillator is sufficiently stable, i.e., the qubit leakages could be safely neglected.

First, against the potential qubit leakages besides the environment noises, the energy level distribution of the trapped electron vibrating along the y-direction might be affected by the strength of the transverse trapping static electric field E_{dc}. However, as shown in Figure 3, the transition frequency ω_a of the qubit changes really with the E_{dc} (red line), which is controllable from 1 GHz to 10 GHz. While, the blue line shows that, the change of the difference between the ω_a and $\omega_{12} = (E_2 - E_1)/\hbar$ is still sufficiently large, i.e., it is almost stable around 27.637 MHz. Here, E_2 is the energy of the third level of the anharmonic oscillator. This indicates that, if the qubit is manipulated by the narrow linewidth (such as a few MHz) microwave pulse in CMW band, then the possible qubit leakage, such as to the state $|2\rangle$, can be suppressed.

Next, we verify that the qubits in a trap array are addressable individually, although the Coulomb interactions between the electrons in different traps are always on. Basically, the high-fidelity single-qubit operation is desirable for the scalable quantum computing on chip. In the present configuration shown typically in Figure 1, the Coulomb interaction of the electrons trapped in two adjacent potentials can be easily expressed as

$$U_{ee} = \frac{e^2}{4\pi\varepsilon_0 S}, \tag{8}$$

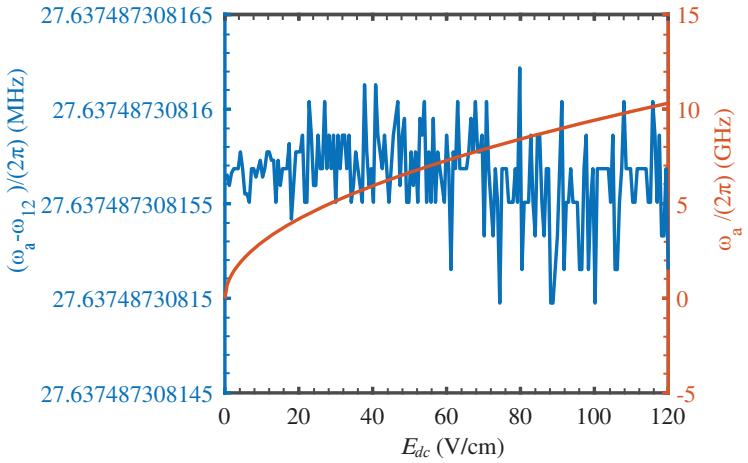

Figure 3. The transition frequency $\omega_a = (E_1 - E_0)/\hbar$ and the difference between ω_a and the transition frequency $\omega_{12} = (E_2 - E_1)/\hbar$ versus the trapping static electric field strength E_{dc}. Here, the red line refers to ω_a (with the unit being GHz) and the blue curve refers to $\omega_a - \omega_{12}$ (with the unit being MHz), and E_j is the energy of the j-th ($j = 0, 1, 2$) created level of the y-direction anharmonic oscillation of the trapped electron.

where $S = Y_{n+1} - Y_n + y_n + y_{n+1}$ is the distance between the electrons with Y_n being the equilibrium position of the electron trapped in the n-th potential, in which the vibrational displacement of the electron away from its equilibrium position is y_n. Experimentally, the distance between the centers of two nearest-neighbor potentials could be set as: $S_y = Y_{n+1} - Y_n \sim 100\ \mu$m, yielding $y_n/S_y \ll 1$. As a consequence, by neglecting the higher-order terms of y_n/S_y, Equation (8) reduces to

$$U_{ee} = \frac{e^2}{4\pi\varepsilon_0(S_y + y_n + y_{n+1})} \approx \frac{e^2}{4\pi\varepsilon_0 S_y}\left[1 + \frac{y_n^2 - y_n S_y}{S_y^2} + \frac{y_{n+1}^2 - y_{n+1}S_y}{S_y^2} + \frac{2y_n y_{n+1}}{S_y^2}\right]. \quad (9)$$

Here, the first term is a c-number term which can be omitted certainly. While, the second and third terms represent the negligible Stark shifts of the levels, induced by the Coulomb interaction. Therefore, the interaction between the electrons trapped in different potentials is mainly determined by the fourth term. In the phonon representation, the Coulomb interaction between the electrons trapped in the nearest-neighbor potentials can be effectively expressed as

$$\hat{H}_{ee} = \frac{2e^2 y_n y_{n+1}}{4\pi\varepsilon_0 S_y^3} \approx \hbar g_{ee}(\hat{c}_n \hat{c}_{n+1}^\dagger + \hat{c}_n^\dagger \hat{c}_{n+1}), \quad (10)$$

under the usual rotating-wave approximation. Here, $\hat{c}_n$ ($\hat{c}_n^\dagger$) is the vibrational Bosonic annihilation (creation) operator of the n-th electron and $[\hat{c}_n, \hat{c}_n^\dagger] = 1$. Above, $g_{ee} \approx e^2/(4\pi\varepsilon_0 m S_y^3 \omega_y)$ is the strength. With the typical parameters, such as $E = 53.87$ V/cm, $S_y \sim 100\ \mu$m, and $\omega_y \sim 2\pi \times 6.9282$ GHz, we get $g_{ee} \sim 2\pi \times 0.926$ KHz. This implies that the Coulomb interaction between the electrons trapped in the nearest-neighbor traps along the y-direction is significantly weak and thus the selected qubit can be addressed individually.

Thirdly, we verify further that, compared with the coupling between the qubit and the CPW-TLR at the bottom of liquid Helium, the Coulomb interaction can be really omitted. In

fact, for a trapped electron moving along the $y-$direction, the dipole interaction between the trapped electron and the lateral quantized electric field [42]

$$\hat{E}_y(y) = \frac{\hat{V}(y)}{h} = \frac{k}{C}\cos(ky)\sqrt{\frac{\hbar}{Ll\omega_r}}(\hat{a}_r + \hat{a}_r^\dagger) \tag{11}$$

can be expressed as

$$\hat{H}_{eR} = ey\hat{E}_y(y). \tag{12}$$

Above, $\hat{a}_r$ ($\hat{a}_r^\dagger$) is the Bosonic annihilation (creation) operator of the CPW-TLR and $[\hat{a}_r, \hat{a}_r^\dagger] = 1$. Also, $\omega_r = 1/\sqrt{CL}$ is the fundamental frequency of the standing electromagnetic field in the CPW-TLR with the wave vector $k = \pi/l$. In the qubit representation spanned by $|0\rangle$ and $|1\rangle$, we have

$$y = (|0\rangle\langle 0| + |1\rangle\langle 1|)\, y\, (|0\rangle\langle 0| + |1\rangle\langle 1|) = \sum_{i,j=0,1} y_{ij}|i\rangle\langle j|, \tag{13}$$

where $\langle i|y|j\rangle = \int \psi_i y \psi_j^* dy$ and $i \neq j = 0, 1$, with $\psi_{i,j}$ being the relevant qubit states. With the typical parameters, one can easily prove that, $y_{01} = y_{10} \sim 3.7 \times 10^{-8} \gg y_{00} \sim 2.3 \times 10^{-22}$, and $y_{11} \sim 3 \times 10^{-22}$. As a consequence, the y-dependent interaction between the qubit and the transverse quantized electric field in the CPW-TLR can be expressed as:

$$\hat{H}_{eR}(y) = \hbar g_{eR}(\hat{a}_r\hat{\sigma}^+ + \hat{a}_r^\dagger\hat{\sigma}^-). \tag{14}$$

Here, $\hat{\sigma}^+ = |1\rangle\langle 0|$ and $\hat{\sigma}^- = |0\rangle\langle 1|$ are the pseudo-spin Pauli operators of the qubit. According to the design in Fig. 1(b), we have $\omega_r \approx 2\pi \times 5.7$ GHz for $l = 11063$ μm, the characteristic impedance $Z_0 \approx 55.4$ Ω, capacitance $C \approx 1.57$ pF, and the inductance $L = 4.82$ nH. If the trap electrodes is set at $y \sim 4900$ μm, the value of the $g_{eR}(y)$-parameter in Eq. (14) can be estimated as: $g_{eR} = [ey_{01}\cos(ky)/h]\sqrt{1/(C^2Ll\hbar\omega_r)} \approx 2\pi \times 14.5$ MHz. This indicates that the qubit-TLR coupling is still sufficiently weak, compared with the qubit leakage frequency, i.e., $\omega_a - \omega_{12} \sim 2\pi \times 27.6$ MHz. However, it is still significantly larger than the Coulomb interaction (i.e., $g_{ee} \sim 2\pi \times 0.926$ KHz) between the electrons in the adjacent traps along the y-direction. Therefore, both the Coulomb interaction between the electrons in different traps and the coupling of the qubit with the CPW-TLR do not lead to the unwanted qubit leakage. Therefore, by using the CPW-TLR as the data bus, the single-qubit operation on the arbitrarily addressable qubit and the switchable interbit operations between the selected qubits can be effectively implemented.

It is valuable to emphasize that, two main points are considered for the chip designs. First, the coupling strength g_{eR} between the trapped electron and the resonator should be less than the leakage difference, e.g., $\omega_a - \omega_{01} \sim 2\pi \times 27.6$ MHz, to satisfy the rotating-wave approximation. As the most electric field strength of the cavity is at the ends of the 1/2-wavelength resonator, and the smallest one is at the middle, the traps are better set as the region near the middle points (for the setting above, $0.393l < y < 0.607l$). Secondly, the inter-electron Coulomb interaction should be much weaker than the indirect coupling between the qubits by using the resonator as a data bus. With the above consideration, we can estimate that at least 20 microelectrodes with a spacing of 100 μm can be set for the cavity with the wavelength of the standing wave being about 2300 μm.

3. The feasibility of the basic quantum gate operations

Given the coupling between the trapped electron and the CPW-TLR is significantly stronger than the Coulomb interaction between the trapped electrons in different potentials, and also the eigenfrequency of the qubit demonstrated above can still be adjusted by controlling the biased electric field via the electrodes at the bottom of the liquid Helium, the desired gate operations can be implemented for quantum computation with the qubit array being shown in Figure 4.

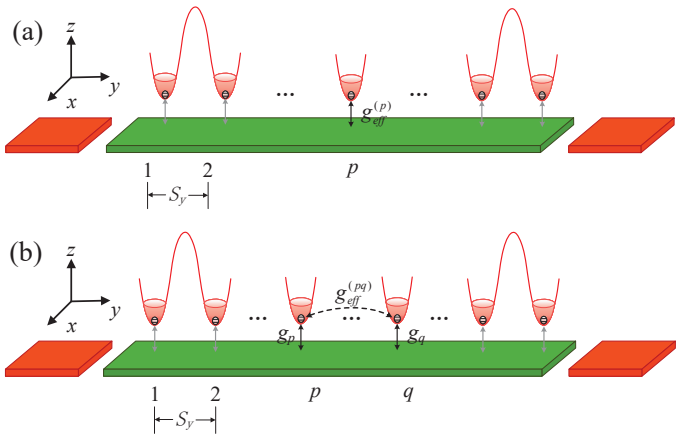

Figure 4. A qubit array is generated by a series of trapped electrons on liquid Helium to implement the desired quantum computation. Here, the qubit is encoded by the ground- and first excited state of the vibration of the trapped electron along the y-direction, and the CPW-TLR is served as the data bus to implement the operation(s) on the addressable qubit(s). The other qubits are adjusted to far-off resonant interaction with the CPW-TLR and thus can not be driven. (a)Individually addressable single-qubit operation on the arbitrarily selected the pth qubit by adjusting its eigenfrequency to implement the resonant interaction with the CPW-TLR. (b) Tunable two-qubit operation on the arbitrarily addressed two qubits, e.g., the p-th- and q-th ones, by using the effective interaction between them.

The well-developed circuit QED technique, used widely for superconducting quantum computation, can be directly applied to implement the desired quantum gate operations with the present system, although certain details are still required to be considered specifically. First, in the circuit QED system the qubit and the cavity are in the same plane, such as the vacuum electric field of the cavity can be directly coupled to the qubit by providing a biased voltage and flux [38]; while, in the present system, the cavity at the bottom of the liquid Helium and the qubits encoded by the lateral orbit states of the trapped electrons are not in the same plane, and thus the qubit-cavity interaction is gotten by the direct electric-dipole one of the electrons in the vacuum electric field. Second, the interaction between the distant qubits in the superconducting circuit QED chip can be switched on/off by either adjusting their detunings with the commonly-coupled cavity or using the switchable couplers. While, in the present system the interbit interaction includes additionally the always-on electron-electron Coulomb couplings, therefore, it is furthermore required to treat these interactions and evaluate their influences on the implementations of high-fidelity single-qubit gate operations. Thirdly, differing from the qubits in the superconducting circuit, the present qubits possess

basically longer decoherence times, as the liquid Helium might isolate most of the circuit noises and thus only the rippons [23] on the liquid Helium surface are the key source of the unwanted decoherence. Therefore, the quantum computation with the present qubits might possess more advantages over that with the superconducting qubits in the circuit QED system, at least the longer durations of the applied pulses can be applied to implement the desired gate operations and the higher-fidelity readouts of the qubit.

3.1. Single-qubit gate operations on the addressed qubit

Let us first discuss the feasibility of the single-qubit operation on the arbitrarily addressable qubit, such as the p-th one, by driving the CPW-TLR, shown schematically in Figure 4(a). As the eigenfrequency ω_a of the qubit can be adjusted individually by controlling the trapping electric fields via the electrodes at the bottom of liquid Helium, and also the influence of the Coulomb interactions between the selected qubit and the other ones in different potentials can be safely neglected, the arbitrarily selected qubit can be addressed by letting it couple to the CPW-TLR, individually. The other qubits are decoupled simultaneously by letting their frequencies be far-off resonance with the CPW-TLR.

The Hamiltonian for driving the CPW-TLR to couple it to the p-th qubit can be written as [43]:

$$\hat{H}_p = \hbar\omega_r\hat{a}_r^\dagger\hat{a}_r + \frac{1}{2}\hbar\omega_p\hat{\sigma}_p^z + \hbar g_p(\hat{a}_r^\dagger\hat{\sigma}_p^- + \hat{a}_r\hat{\sigma}_p^+) + \hbar\hat{a}_r\xi^* e^{i\omega_d t} + \hbar\hat{a}_r^\dagger\xi e^{-i\omega_d t}. \tag{15}$$

where $\sigma_p^z = |1\rangle\langle 1| - |0\rangle\langle 0|$, σ_p^+ and σ_p^- are the pseudo-spin Pauli operators of the p-th qubit. Here, the first and the second terms are the free Hamiltonians of the quantized microwave standing wave field in the CPW-TLR and the selected qubit, respectively. The third term refers to the interaction between the qubit and the CPW-TLR under the usual rotating wave approximation, wherein the strength $g_p = g_{eR}(y_p)$ depends on the location of the p-th qubit; the last two terms describe the microwave drive of the CPW-TLR with ω_d and ξ being the driving frequency and strength, respectively. Interestingly, the Hamiltonian (15) undergoes an evolution (see Appendix B):

$$U_p(t) = \begin{pmatrix} \cos\left[\frac{A(t)}{2}\right] & -i\sin\left[\frac{A(t)}{2}\right] \\ -i\sin\left[\frac{A(t)}{2}\right] & \cos\left[\frac{A(t)}{2}\right] \end{pmatrix}, \tag{16}$$

which is nothing but a single-qubit operation of the p-th qubit. By adjusting the driving strength $\alpha(t)$ and the driving time t, various single-qubit state manipulations can be specifically achieved. For example, if $A(t) = \pi$, then the single-qubit X gate: σ_p^X, can be realized; while if $A(t) = \pi/2$, then the Hadamard gate operation on the p-th qubit can be realized. Actually, if the frequency of another qubit is set as $\omega_{ot} = 10$ GHz, the effective couple strength $g_{ot}^2/(\omega_{ot} - \omega_r)$ between it and CPW-TLR reads ~ 0.21 MHz, which is much less than $g_{eR}^2/(\omega_p - \omega_r) \sim 1.1$ MHz. Therefore, the coupling between the driven CPW-TLR and the other qubits can be effectively neglected by engineering their frequencies to be far-off resonances by controlling their static electric field biases.

3.2. Two-qubit logic gate on a pair of arbitrarily selected qubits

Next, we investigate how to implement the two-qubit operation between a pair of arbitrarily qubits by using the tunable inter-qubit interaction achieved by using the simultaneously coupling them to the data bus, i.e., the CPL-TLR. As shown in Figure 4(b), the p-th and q-th of the frequencies ω_p and ω_q, with the negligible Coulomb interaction, are addressed to simultaneously couple to the CPW-TLR. The Hamiltonian for such an operation reads

$$\hat{H}_{do} = \hbar\omega_r \hat{a}_r^\dagger \hat{a}_r + \frac{1}{2}\hbar\omega_p \hat{\sigma}_p^z + \frac{1}{2}\hbar\omega_q \hat{\sigma}_q^z + \hbar g_p(\hat{a}_r^\dagger \hat{\sigma}_p^- + \hat{a}_r \hat{\sigma}_p^+) + \hbar g_q(\hat{a}_r^\dagger \hat{\sigma}_q^- + \hat{a}_r \hat{\sigma}_q^+), \tag{17}$$

where σ_q^z, σ_q^+ and σ_q^- are the pseudo-spin Pauli operators of the q-th qubit. g_p and $g_q = g_{eR}(y_q)$ are dependent of the locations of the qubits. Under the conditions: $g_p \ll \Delta_p$, and $g_q \ll \Delta_q = |\omega_q - \omega_r|$, the Hamiltonian (17) can be effectively written as:

$$\begin{aligned}\hat{H}'_{do} =& \hbar(\omega_r + \chi_p \hat{\sigma}_p^z + \chi_q \hat{\sigma}_p^z)\hat{a}_r^\dagger \hat{a}_r + \frac{1}{2}\hbar(\omega_p + \chi_p)\hat{\sigma}_p^z + \\ & \frac{1}{2}\hbar(\omega_q + \chi_q)\hat{\sigma}_p^z + \hbar g_{pq}(\hat{\sigma}_p^- \hat{\sigma}_q^+ + \hat{\sigma}_p^+ \hat{\sigma}_q^-),\end{aligned} \tag{18}$$

where $\chi_p = 2g_p^2/\Delta_p$, $\chi_q = 2g_q^2/\Delta_q$, and

$$g_{eff}^{(pq)} = \frac{g_p g_q(\Delta_p + \Delta_q)}{\Delta_p \Delta_q} \tag{19}$$

is the effective interaction between the distant qubits. Above, the second- and higher orders of g_p/Δ_p and g_q/Δ_q are ignored. It indicates that an effective interaction $g_{eff}^{(pq)}$ between the p-th- and q-th qubits without the direct interaction, can be obtained by using the CPL-TLR as the data bus.

Specifically, if $\Delta_q = \Delta_p = \Delta$, and $g_p = g_q = g$, then the effective coupling Hamiltonian between the distant qubits can be abbreviated as:

$$\hat{H}_{qp} = \frac{2\hbar g^2}{\Delta}(\hat{\sigma}_p^- \hat{\sigma}_q^+ + \hat{\sigma}_p^+ \hat{\sigma}_q^-), \tag{20}$$

in the interaction picture. It delivers the following evolution operator:

$$\begin{aligned}U_{qp}(t) = \exp(-\frac{i}{\hbar}\hat{H}_{qp}t) &= \sum_{n=0}^{\infty} \frac{(-i\kappa t)^n}{n!}(\hat{\sigma}_p^- \hat{\sigma}_q^+ + \hat{\sigma}_p^+ \hat{\sigma}_q^-)^n \\ &= \begin{pmatrix} 1 & 0 & 0 & 0 \\ 0 & \cos(\kappa t) & -i\sin(\kappa t) & 0 \\ 0 & -i\sin(\kappa t) & \cos(\kappa t) & 0 \\ 0 & 0 & 0 & 1 \end{pmatrix},\end{aligned} \tag{21}$$

with $\kappa = 2g^2/\Delta$. Obviously, when the evolution time is controlled as $t = \pi/(2\kappa)$, a two-qubit i-SWAP gate operation between the distant qubits can be realized. It is emphasized that the effective coupling between the selected two qubits could be realized. One can see from

Equation (20) that, the effective interaction between the qubits can be engineered by adjusting the eigenfrequencies of the qubits and consequently the detunings between them the TLR. For instance, by setting $\omega_p = \omega_q = 2\pi \times 6.9$ GHz, the virtual interaction strength between two qubits can be obtained as $g_{eff}^{(pq)} \sim 4.2$ MHz, which is significantly stronger than the Coulomb interaction between the two trapped electrons.

Certainly, the implementation of the desired high-fidelity two-qubit gates is required to suppress the cross-talks from the other qubits. For example, the influence from the third qubit, says the sth one, on the fidelity of the desired two-qubit gate operation between the selected p-th and q-th ones. This is certainly feasible, at least theoretically, by setting the eigenfrequency of the s-th qubit to be large detuning from the selected qubits. Neglecting all the significantly-weak Coulomb interactions, the Hamiltonian for the coupled three-qubits system, say p, q, and s, by the common CPW-TLR, can be specifically written as

$$\begin{aligned}\hat{H}_{tri} =&\hbar\omega_r\hat{a}_r^{\dagger}\hat{a}_r 1 + \frac{1}{2}\hbar\omega_p\hat{\sigma}_p^z + \frac{1}{2}\hbar\omega_s\hat{\sigma}_s^z + \frac{1}{2}\hbar\omega_q\hat{\sigma}_q^z \\ &+ \hbar g_p(\hat{a}_r^{\dagger}\hat{\sigma}_p^- + \hat{a}_r\hat{\sigma}_p^+) + \hbar g_s(\hat{a}_r^{\dagger}\hat{\sigma}_s^- + \hat{a}_r\hat{\sigma}_s^+) + \hbar g_q(\hat{a}_r^{\dagger}\hat{\sigma}_q^- + \hat{a}_r\hat{\sigma}_q^+).\end{aligned} \tag{22}$$

Under the condition: $g_s/\Delta_s, g_p/\Delta_p, g_q/\Delta_q \ll 1$, it can be effectively rewritten as:

$$\hat{H}_{tri}^I = \hbar g_{ps}(\hat{\sigma}_p^-\hat{\sigma}_s^+ + \hat{\sigma}_p^+\hat{\sigma}_s^-) + \hbar g_{pq}(\hat{\sigma}_p^-\hat{\sigma}_q^+ + \hat{\sigma}_p^+\hat{\sigma}_q^-) + \hbar g_{sq}(\hat{\sigma}_s^-\hat{\sigma}_q^+ + \hat{\sigma}_s^+\hat{\sigma}_q^-), \tag{23}$$

in the interaction picture, where

$$g_{eff}^{(ps)} = \frac{g_p g_s(\Delta_p + \Delta_s)}{\Delta_p\Delta_s},\ g_{eff}^{(sq)} = \frac{g_s g_q(\Delta_s + \Delta_q)}{\Delta_s\Delta_q}, \tag{24}$$

and $\Delta_s = |\omega_s - \omega_r|$. Therefore, the influence of the s-th qubit, on the fidelity of the desired two-qubit iSWAP gate operation between the selected p-th and q-th ones, can be numerically checked the state evolution of the three-qubit system using the time-evolution operator $U_{tri} = \exp(-\frac{\mathrm{i}}{\hbar}\hat{H}_{tri}^I t)$. Specifically, Fig. 5 shows how the populations of the state $|001\rangle$ change with the different pulse durations. For $\omega_s = 2\pi \times 10$ GHz and $g_{eff}^{(ps)} \sim 2.2$ MHz, One can see that, if the microwave pulse duration is still set as $t = \pi/(2g_{eff}^{pq})$ expected previously to achieve the ideal two-qubit i-SWAP gate operation between the p-th and q-th qubits, the populations read 0.08 for the state $|001\rangle$, 0.34 for the state $|010\rangle$, and 0.58 for the state $|100\rangle$, respectively. This indicates that the fidelity of the i-SWAP gate is lowered manifestly as 58%. However, if the duration of the applied is enlarged as 0.927μs, then the fidelity of the two-qubit i-SWAP gate can be further enhanced up to 94.1%. Figure 5(b) shows clearly that, such a fidelity can be significantly enhanced, e.g., up to 99.99%, if the detuning between the s-th qubit and the $p - /q-$th qubit can be further enlarged. Therefore, by enhancing the detunings between the selected qubit and the other ones and properly setting the duration of the applied microwave pulse, the desired two-qubit gate operations can be implemented with high fidelities, even if the other qubits are practically in the presence.

Theoretically, with the combination of the single-qubit operations on the arbitrarily addressable qubits and a tunable two-qubit quantum logic gate operation on the arbitrarily selected two qubits, any quantum operation can be achieved to implement the desired quantum

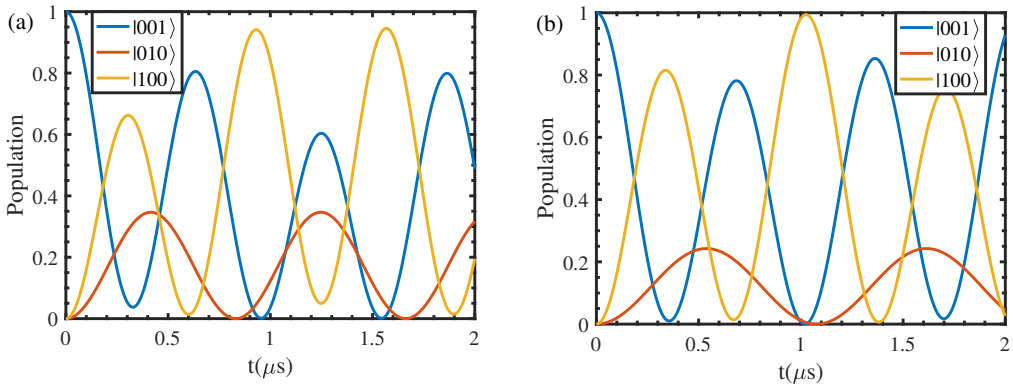

Figure 5. Numerical simulations of the population evolutions of the two-qubit i-SWAP gate operation: $|001\rangle \leftrightarrow |100\rangle$, under the presence of the middle qubit prepared initially at the state $|0\rangle$. The blue, red, and yellow lines refer to the states $|001\rangle$, $|010\rangle$, and $|100\rangle$, respectively. Here, the eigenfrequencies of the first and third qubits are set as $\omega_p/(2\pi) = \omega_q/(2\pi) = 6.9$ GHz, while that of the second qubit, i.e, the middle one, is set as $\omega_s/(2\pi) = 10$ GHz (a) and $\omega_s/(2\pi) = 17.7$ GHz (b), respectively.

computation. Therefore, with the quantum gate operations demonstrated above, quantum computation with the qubits encoded by the lateral vibrations of the trapped electrons on liquid Helium is feasible.

4. Numerical confirmation of the QND readouts of the qubits

Finally, we demonstrate the quantum non-demolition (QND) readout(s) of the arbitrarily selected qubit(s) by numerical simulations. The approach proposed here is significantly different from the one proposed previously for the longitudinally moving qubit (i.e., Hydrogen-like ones) [20, 24, 44], wherein a readout pulse should be applied to lower the longitudinal potential for measuring the tunneling current of the trapped electron on liquid Helium. In fact, due to the controllable dispersive interaction, the QND measurements of the arbitrarily selected qubit can be implemented by probing the transmission of the driving microwave. This method has been widely applied to various solid-state circuit QED systems [45–49] and should also be feasible for the present one.

Specifically, the QND readout the p-th qubit, , by using the microwave to drive the dispersively coupled CPW-TLR, can be described by the following Hamiltonian [50]:

$$\begin{aligned}\hat{H}_p =& \frac{1}{2}\hbar\omega_p\hat{\sigma}_p^z + \hbar\omega_r\hat{a}_r^\dagger\hat{a}_r + \frac{\hbar g_p^2}{\triangle_p}\hat{a}_r^\dagger\hat{a}_r\hat{\sigma}_p^z + \sum_{n=1,2}\int_{-\infty}^{+\infty}\hbar\omega_n d\omega_n\hat{b}_n^\dagger(\omega_n)\hat{b}_n(\omega_n) \\ &+ \mathrm{i}\hbar\sum_{n=1,2}\int_{-\infty}^{+\infty} d\omega_n\lambda_n(\omega_n)\left[\hat{a}_r\hat{b}_n^\dagger(\omega_n) - \hat{a}_r^\dagger\hat{b}_n(\omega_n)\right],\end{aligned} \tag{25}$$

where $b_n(\omega_n)$ $(n = 1, 2)$ and $b_n^\dagger(\omega_n)$ are the operators of the applied microwave pulse with the frequency ω_n, λ_n is the interaction strength between it and CPW-TLR, the detected qubit is dispersively coupled to the driven CPW-TLR and thus $\triangle_p \gg g_p$.

For the detection, the dissipation rate of the qubit is assumed to be sufficiently lower than that of the driven CPW-TLR, and thus the qubit dissipation is negligible during its readout, i.e., $\hat{\sigma}_p^z(t) = \hat{\sigma}_z(0)$ in Heisenberg picture to keeps the population of the qubits is unchanged during the readout.

4.1. Frequency domain measurement simulations

Using the standard input-output theory [50], the transmission coefficient of the microwave-driven CPW-TLR can be easily calculated as:

$$t_p(\omega) = \frac{\sqrt{\gamma_1\gamma_2}}{\frac{1}{2}(\gamma_1+\gamma_2) + \mathrm{i}[\frac{g_p^2}{\triangle_p}\langle\sigma_p^z(0)\rangle - (\omega-\omega_r)]}. \tag{26}$$

where $\gamma_n = 2\pi\lambda_n^2$ is the dissipation of bilateral mirrors of the resonator cavity. It is seen from Figure 6 that, compared with spectrum of the empty cavity (EMC) peaked at $\omega = \omega_r$, if the qubit is in the ground (excited) state, the peak of the transmitted spectrum is shifted right (left) to $\omega_{|1_p\rangle} = \omega_r + g_p^2/\triangle_p = 6.8$ MHz ($\omega_{|0_p\rangle} = \omega_r - g_p^2/\triangle_p = 4.6$ MHz) [48]. This is the usual vacuum Rabi splitting of the cavity due to the existence of a two-level system.

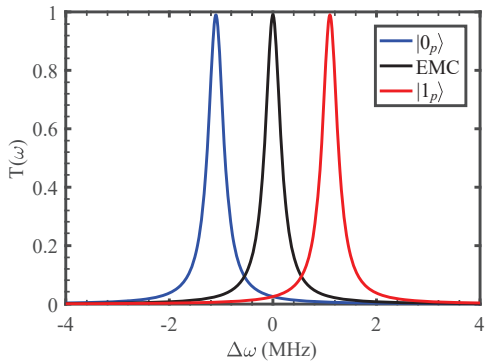

Figure 6. Microwave transmission spectra of the driven CPW-TLR dispersively coupled to the detected q-th qubit, whose different states lead to the different shifts of the peak. Here, the black line refers to the EMC, and the blue (red) line peaked at $\triangle\omega_{|0_p\rangle} = -g_p^2/\triangle_p = -1.1$ GHz ($\triangle\omega_{|1_p\rangle} = g_p^2/\triangle_p = 1.1$ GHz) corresponding to the qubit is in the ground (excited) state. The relevant parameters are set as: $\omega_p/(2\pi) = 6.9$ GHz and $\omega_r/(2\pi) = 5.7$ GHz, $g_p/(2\pi) = 14.5$ MHz, $\gamma_1/(2\pi) = 25.65$ KHz, and $\gamma_2/(2\pi) = 31.35$ KHz, respectively.

The transmission spectra shown in Figure 6 are obtained by assuming that the qubit is in either the state $|0_p\rangle$ or the state $|1_p\rangle$, respectively. However, the reality is that, the qubit state is unknown before the detection, i.e., $|\psi_p\rangle = \alpha_p|0_p\rangle + \beta_p|1_p\rangle$, $|\alpha_p|^2 + |\beta_p|^2 = 1$ with α_p and β_p being measured. It implies that, after repeated detections of the multiple samples of a common unknown quantum state, the number of the observed peak at $\omega_{|1_p\rangle}$ ($\omega_{|0_p\rangle}$) should be proportional to the superposition probability $|\alpha_p|^2$ ($|\beta_p|^2$) [51–54]. Therefore, by reading the normalized height of the corresponding transmitted peak, the coefficients of the superposed computational states in an unknown state of the p-th qubit could be measured. This argument is verified again by the numerical simulations shown in Figure 6, wherein the normalized

spectra of the driven CPW-TLR are given specifically for the p-th qubit prepared in different superposed states.

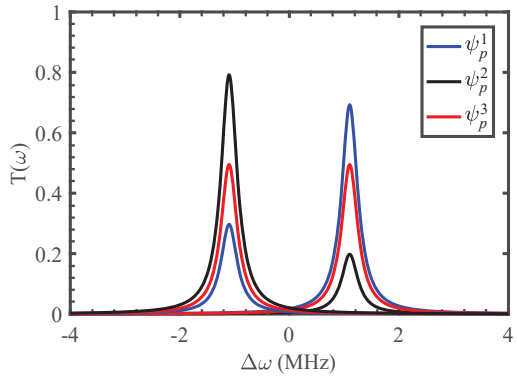

Figure 7. The normalized transmitted spectra of the driven CPW-TLR dispersively coupled to the qubit, which is prepared in the different superposed states: $|\psi_p^1\rangle = \sqrt{0.3}|0\rangle + \sqrt{0.7}|1\rangle$ (blue), $|\psi_p^2\rangle = \sqrt{0.8}|0\rangle + \sqrt{0.2}|1\rangle$ (black), and $|\psi_p^3\rangle = \sqrt{0.5}|0\rangle + \sqrt{0.5}|1\rangle$ (red). Here, the relevant parameters are set as the same as in Figure 6.

In a nutshell, the QND readout of the selected p-th qubit, by probing the transmissions of the driven CPW-TLR, can be performed as the follows.

i) If the transmitted peak is observed at the center frequency ω_r of the CPW-TLR, then the p-th qubit decouples from the driven TLR. The qubit readout fails, and then the detuning between the qubit and the cavity is required to be adjusted by changing the eigenfrequency of the qubit until the shift of the transmitted peak is obtained.

ii) If all the observed peaks are shifted rightly into a common location, then we know that the read qubit is surely in the excited state $|1_p\rangle$; otherwise, it is in the ground state $|0_p\rangle$. From the shift quantity, the qubit-TLR effective interaction g_p^2/Δ_p can be determined.

iii) During a series of the repeated detections for the same samples, if the peaks shifted rightly are observed in some events and the right shifts in the other events, then one can argue that the qubit is in a superposed state. The superposition coefficients $|\beta_p|^2$ and $|\alpha_p|^2$ can be determined by the relative heights of the peaks in the normalization spectra, which correspond to the populations of the state $|1_p\rangle$ and $|0_p\rangle$, respectively.

Immediately, the frequency domain measurement method demonstrated above provides an easy way to judge whether the qubit is in either a coherent pure state or a mixed one. In fact, the above transmitted spectral method determines only the populations of the qubit states $|1_p\rangle$ and $|0_p\rangle$. This implies that it can not directly differentiate the maximally mixed state: $\rho_{mix} = (|0_p\rangle\langle 0_p| + |1_p\rangle\langle 1_p|)/2$ from a coherent pure state $\rho_{pur} = (|0_p\rangle + |1_p\rangle)(\langle 0_p| + \langle 1_p|)/2$, since both the states cause the same shifts in the spectra. This problem can be easily overcome as follows. Before the spectral detections, a Hadamard gate operation $U_H = (|0_p\rangle\langle 0_p| - |1_p\rangle\langle 1_p| + |0_p\rangle\langle 1_p| + |1_p\rangle\langle 0_p|)/\sqrt{2}$ is applied to the qubit, and then perform the measurements of the transmitted spectra of the driven CPW-TLR. As shown in Figure 8, if the qubit state is beforehand in the state ρ_{mix}, the spectra with the two peaks are unchanged; on the contrary, if the qubit state is beforehand in the state ρ_{pur}, then only one peak, refers

to the state $|0_p\rangle$, can be observed. Therefore, the proposed frequency-domain measurement method can also be applied to realize the purity test of the qubit.

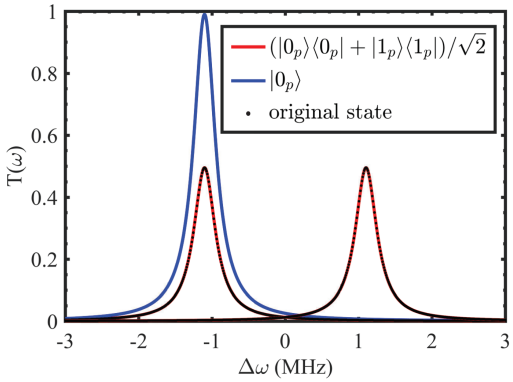

Figure 8. After the Hadamard gate operation, qubits in different states of the maximum mixed state or the maximum coherent superposition state affect the transmission spectrum of the driven CPW-TLR, resulting in different normalized microwave transmission spectra: the red line (the two peaks of equal height correspond to the two states of the qubit) indicates that the original qubit is in the maximum mixed state; while the blue line (single peak) indicates that the original qubit state is the maximum coherent superposition state. Here, the relevant parameters are set as the same as in Figure 6.

4.2. Time domain measurement simulations

Unlike the above frequency domain measurements, which require the scanning of the frequency of the driving microwave, below we discuss how to implement the time domain detections of the qubit by using the usual IQ-mixing technique. By which the timely readout of the selected qubit can be achieved by probing the qubit-induced scattering signal of the cavity at a selected frequency (typically such as the resonant driving signal with the frequency $\omega_d = \omega_r = \omega_{LO}$).

The IQ-mixing technique is usually performed as follows. First, a microwave signal $E_{LO} = A_{LO}\sin(\omega_{LO}t)$, with a known frequency and amplitude, is divided into two channels by a power divider; one is served as the local coherent signal, and the other is used to drive the CPW-TLR for the detection. Next, if the TLR is coupled to the qubit wanted to be readout, then its transmitted signal reads: $E_{out}(t) = A_i\cos(\omega_{LO}t + \phi_i)$ $(i = 0, 1)$, depending on the states of the qubit. Finally, by mixing the local- and transmitted signals, the qubit-induced changes, i.e., A_i and ϕ_i, can be determined as:

$$A_i = \left|\frac{\langle\hat{a}_{out}^{(2)}\rangle}{\langle\hat{a}_{in}^{(1)}\rangle}\right|,\ \phi_i = \arctan\left(\frac{\langle\hat{a}_{out}^{(2)}\rangle}{\langle\hat{a}_{in}^{(1)}\rangle}\right). \tag{27}$$

They can be detected by probing the signals at the I-part outport [55]:

$$S_I = E_{LO}^{(1)} \times E_{out}^{(I)} = \frac{A_{LO}}{\sqrt{2}}\cos(\omega_{LO}t) \times \frac{A_i}{\sqrt{2}}\cos(\omega_{LO}t + \phi_i) \approx \frac{A_{LO}A_i}{4}\cos\phi_i, \tag{28}$$

and the Q-part one:

$$S_Q = E_{LO}^{(2)} \times E_{out}^{(Q)} = \frac{A_{LO}}{\sqrt{2}} \sin(\omega_{LO} t) \times \frac{A_i}{\sqrt{2}} \cos(\omega_{LO} t + \phi_i) \approx \frac{A_{LO} A_i}{4} \sin\phi_i, \tag{29}$$

simultaneously. Above, the high-frequency signals generated by the mixer are filtered out.

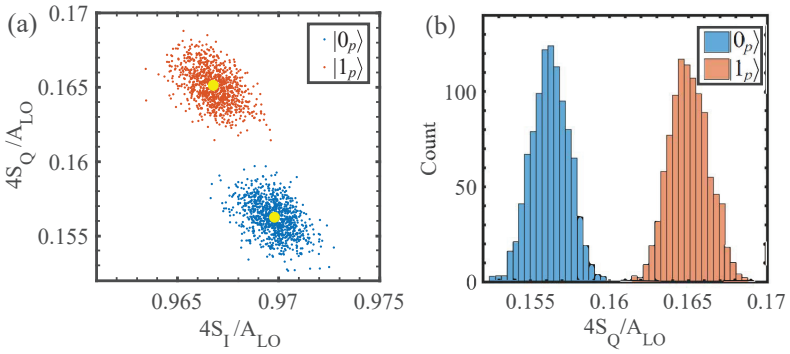

Figure 9. Simulation of time-domain measurements of the selected p-th qubit by using the IQ-mixing technique: (a) the distribution of the measured signals on the I-Q plane; the blue (red) dots refer to the qubit in the ground state $|0_p\rangle$ (the excited state $|1_p\rangle$), wherein the yellow dots correspond to the ideal distributions; (b) the statistical distribution of the measured I-Q signals shows that, for the same measurement samples, the heights of the statistical peaks are basically the same. Here, each parameter is taken as: $\gamma_1/(2\pi) = 25.65$ KHz, $\gamma_2/(2\pi) = 31.35$ KHz, $\omega_r/(2\pi) = 5.7$ GHz, $\omega_p/(2\pi) = 6.9$ GHz and $g_p/(2\pi) = 14.5$ MHz.

Certainly, noise always exists in the actual experimental measurements and thus affects the measurement accuracies of the I and Q signals, thereby affecting the readout fidelity of the qubit. Figure 9 numerically simulates how the statistical distributions of the measured I-Q signals for 1000 measurements on a given qubit state. It is seen that when the qubit is prepared at the $|0_p\rangle$-state, the signal amplitudes are basically distributed near a yellowed center point located at (S_I, S_Q)=(0.9668, 0.1651); while, if the qubit state is prepared at the $|1_p\rangle$-state, the signal amplitudes are alternatively distributed around another yellowed center point located at $(S_I, S_Q) = (0.9698, 0.1562)$.Correspondingly, Figure 9(b) shows that, if the qubit is prepared at either the state $|1_p\rangle$ or $|0_p\rangle$, the number of the events that the measured (I, Q) values near one of the yellowed center points is almost the same.

Consequently, for an unknown qubit state, the population of the state $|0_p\rangle$ ($|1_p\rangle$) can be determined by the number of the events whose (S_I, S_Q) located around the two yellowed points in the I-Q plane, one refers to the state $|0_p\rangle$ and another refers to the state $|0_p\rangle$. Figure 10(a) shows the simulations of 2000 repeated time-domain QND measurements for the same samples wherein the populations of the two states of the qubit are almost the same, arguing that the qubit is prepared at either the maximal mixture of the qubit states: ρ_{mix}, or the coherent superposition of the qubit states: $\rho_{pur} = (|0_p\rangle + |1_p\rangle)(\langle 0_p| + \langle 1_p|)/2$. Figure 10(b) shows that, after a Hadamard gate operation, the populations of the qubit states are almost unchanged, if it is beforehand prepared at the state ρ_{mix}; while, if the qubit is beforehand at the state ρ_{pur}, then after the Hadamard gate operation, the number of events, in which the I-Q

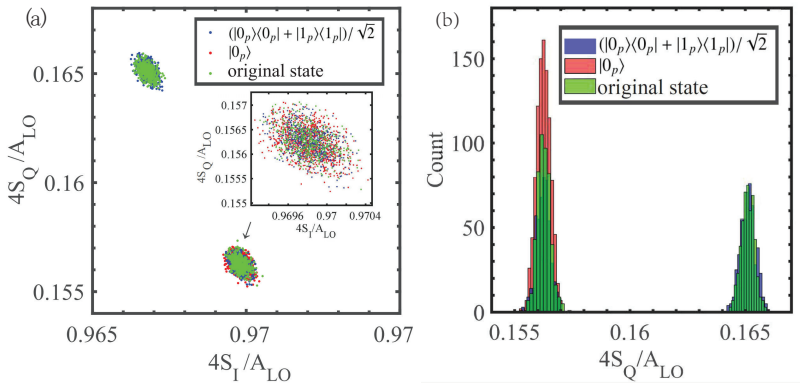

Figure 10. Numerical simulations of the readouts of the p-th qubit in the time domain: (a) the populations of the states $|0_p\rangle$ and $|1_p\rangle$ are almost the same; (b) after the Hadamard gate operation, the mixture state ρ_{mix} of the qubit and the coherent superposition of the qubit's state ρ_{pur} can be distinguished well. The populations are almost unchanged for ρ_{mix}, but that of one of the qubit states vanished for the state ρ_{pur}. Here, various relevant parameters are taken as the same as in Figure 9.

signals fall around the yellowed center point marking the state $|0_p\rangle$, is significantly reduced and most of them distribute near the yellowed center point referred to the state $|1_p\rangle$.

Experimentally, both the frequency-domain and time-domain QND measurement of the qubit can be implemented, if the dissipation time of the detected qubit is significantly longer than the transmitted one of the driving microwave through the TLR, which should possess the sufficiently high quality factor and the sufficiently wide linear region [56].

5. Conclusion and discussion

Given the quantum computation with the qubits encoded by the longitudinal Hydrogen-like motions of the electrons trapped on liquid Helium, by using the microwave drivings in the MMW band, is relatively hard to implement, in this paper we propose an approach to implement the quantum computation alternatively with the qubits encoded by the nonlinear lateral vibrations of the electrons trapped on liquid Helium. We demonstrate that the eigenfrequency of the qubit encoded by the ground- and first excited state of the nonlinear lateral vibration of the trapped electron is in the CMW band, rather than the MMW one in the previous scheme by encoding the qubit into the two lowest Hydrogen-like atom levels. Thus the usual technique used widely in the circuit QED systems can also be directly applied to manipulate the present qubits. The stability of such a qubit, against the perturbations of the electron-electron Coulomb interactions and the qubit-TLR interaction, had been analyzed, in detail. Interestingly, we show that the scheme is scalable, i.e., a qubit array can be generated by using the classical excitation of the CPW-TLR at the bottom of the liquid Helium to implement the traps of a series of electrons on liquid Helium. Furthermore, with the quantized field in the CPW-TLR as the data bus, an arbitrarily selected qubit can be individually addressed to implement the single-qubit operation, and the effective interaction between a pair of arbitrarily selected qubits can be tunable engineered for the implementation

of two-qubit quantum gate operation. Also, the CPW-TLR can be served as the detector for the implementation of the QND measurements of the qubit in both the frequency- and time domains. By the relevant numerical simulations, we demonstrated that the quantum computation with the arrayed qubits generated by the nonlinear lateral vibrations of the electrons on liquid Helium is possible, at least theoretically.

For the experimental realization, a series of setups have been built to implement the trap of the electrons on liquid Helium, in a confined three-dimensional space, and even on the solid Neon [45]. Specifically, it has been demonstrated experimentally that the lateral vibration parallel to the Helium surface is nonlinear and thus can be used to encode the qubit [24]. Also, the electron trap on liquid Helium can be integrated with a superconducting coplanar cavity device onchip, and the MHz-order coupling strength (which is much larger than the resonator linewidth) had been experimentally demonstrated. Moreover, the duration ($\pi/(2\kappa)$) of the proposed π-pulse for the implementation of the two-qubit operation is estimated at the μs-order, which is really feasible. Typically, if the intensity of the static electric field is set as 5387 V/m, and the width of the electrode is 100um, then the static voltage for trapping the electron can be calculated as ~ 0.5387 V. It is really doable. In addition, let the chip be worked at a temperature of ~ 15 mK, the frequency of the strongest thermal noise is estimated as ~ 0.3 GHz, which is significantly less than the transition frequency of the qubit. Thus, the environment thermal noise would not cause the operational false of the qubit. Hopefully, the scheme proposed here to implement the quantum computation with the trapped electrons on liquid Helium could be experimentally realized, in future.

Acknowledgment

This work was partially supported in part by the National Natural Science Foundation Grants NO. 11974290, and the National Key Research and Development Program of China under Grant No. 2021YFA0718803.

Appendix A. From Equation (1) to Equation (2)

Equation (1) can be rewritten as:

$$U(x,y,z) = -\frac{\Lambda e^2}{4\pi\varepsilon_0 z} + eE(t)r, \tag{A.1}$$

with

$$r = \sqrt{(h+z)^2 + x^2 + y^2} = h\sqrt{(1+\tilde{z})^2 + \tilde{x} + \tilde{y}} = hf(\tilde{x},\tilde{y},\tilde{z}), \tag{A.2}$$

where $(x/h)^2 = \tilde{x}$, $(y/h)^2 = \tilde{y}$, $z/h = \tilde{z}$. As $h \gg x, y, z$, the function $f(\tilde{x},\tilde{y},\tilde{z})$ can be expanded as the Taylor series (up to the second order):

$$\begin{aligned} f(\tilde{x},\tilde{y},\tilde{z}) =& f(\tilde{x}_0,\tilde{y}_0,\tilde{z}_0) + f'_{\tilde{x}}(\tilde{x}_0,\tilde{y}_0,\tilde{z}_0)(\tilde{x}-\tilde{x}_0) + f'_{\tilde{y}}(\tilde{x}_0,\tilde{y}_0,\tilde{z}_0)(\tilde{y}-\tilde{y}_0) + f'_{\tilde{z}}(\tilde{x}_0,\tilde{y}_0,\tilde{z}_0)(\tilde{z}-\tilde{z}_0) \\ &+ \frac{f''_{\tilde{x}}(\tilde{x}_0,\tilde{y}_0,\tilde{z}_0)}{2!}(\tilde{x}-\tilde{x}_0)^2 + \frac{f''_{\tilde{y}}(\tilde{x}_0,\tilde{y}_0,\tilde{z}_0)}{2!}(\tilde{y}-\tilde{y}_0)^2 + \frac{f''_{\tilde{z}}(\tilde{x}_0,\tilde{y}_0,\tilde{z}_0)}{2!}(\tilde{z}-\tilde{z}_0)^2. \end{aligned} \tag{A.3}$$

At $(\tilde{x}_0, \tilde{y}_0, \tilde{z}_0) = (0, 0, 0)$, we have

$$\begin{aligned}
f(0,0,0) =& 1, \\
f'_{\tilde{x}}(0,0,0) =& \frac{1}{2}[(1+\tilde{z})^2 + \tilde{x} + \tilde{y}]^{-\frac{1}{2}}|_{(0,0,0)} = \frac{1}{2}, \\
f'_{\tilde{y}}(0,0,0) =& \frac{1}{2}[(1+\tilde{z})^2 + \tilde{x} + \tilde{y}]^{-\frac{1}{2}}|_{(0,0,0)} = \frac{1}{2}, \\
f'_{\tilde{z}}(0,0,0) =& \frac{1}{2}[(1+\tilde{z})^2 + \tilde{x} + \tilde{y}]^{-\frac{1}{2}} \cdot 2(1+\tilde{z})|_{(0,0,0)} = 1, \\
\frac{f''_{\tilde{x}}(0,0,0)}{2} =& -\frac{1}{8}[(1+\tilde{z})^2 + \tilde{x} + \tilde{y}]^{-\frac{3}{2}}|_{(0,0,0)}\tilde{x}^2 = -\frac{1}{8}, \\
\frac{f''_{\tilde{y}}(0,0,0)}{2} =& -\frac{1}{8}[(1+\tilde{z})^2 + \tilde{x} + \tilde{y}]^{-\frac{3}{2}}|_{(0,0,0)} = -\frac{1}{8}, \\
\frac{f''_{\tilde{z}}(0,0,0)}{2} =& \{-\frac{1}{8}[(1+\tilde{z})^2 + \tilde{x} + \tilde{y}]^{-\frac{3}{2}} \cdot 4(1+\tilde{z})^2 + \frac{1}{2}[(1+\tilde{z})^2 + \tilde{x} + \tilde{y}]^{-\frac{1}{2}}\}|_{(0,0,0)} = 0.
\end{aligned}$$

Therefore,

$$r = h(1 + \tilde{z} + \frac{\tilde{x}}{2} - \frac{\tilde{x}^2}{8} + \frac{\tilde{y}}{2} - \frac{\tilde{y}^2}{8}) = \frac{8h^4 + 8h^3 z + 4h^2x^2 - x^4 + 4h^2y^2 - y^4}{8h^3}. \tag{A.4}$$

Substituting it into Equation (1), we get Equation (2) directly.

Appendix B. Derivation of Equation (16)

In a rotating coordinate system with the driving frequency ω_d, the Hamiltonian (15) can be rewritten as:

$$\tilde{H}_p = \hbar\triangle_{rd}\hat{a}_r^\dagger\hat{a}_r + \frac{1}{2}\hbar\triangle_{pd}\hat{\sigma}_p^z + \hbar g_p(\hat{a}_r^\dagger\hat{\sigma}_p^- + \hat{a}_r\hat{\sigma}_p^+) + \hbar\hat{a}_r\xi^* + \hbar\hat{a}_r^\dagger\xi, \tag{B.1}$$

where $\triangle_{rd} = |\omega_r - \omega_d|$, $\triangle_{pd} = |\omega_p - \omega_d|$. Furthermore, under the unitary transformation [43]:

$$D(\alpha) = \exp[\alpha^*(t)\hat{a}_r - \alpha(t)\hat{a}_r^\dagger],\ i\dot{\alpha}(t) + \triangle_{rd}\alpha(t) + \xi(t) = 0,$$

Hamiltonian (B.1) can be transformed into

$$\begin{aligned}
\hat{H}'_p =& DHD^\dagger - i\hbar\frac{\partial D}{\partial t}D^\dagger \\
=& \hbar\triangle_{rd}\hat{a}_r^\dagger\hat{a}_r + \frac{1}{2}\hbar\triangle_{pd}\hat{\sigma}_p^z + \hbar g_p(\hat{a}_r^\dagger\hat{\sigma}_p^- + \hat{a}_r\hat{\sigma}_p^+) + \hbar g_p[\alpha^*(t)\hat{\sigma}^- + \alpha(t)\hat{\sigma}^+].
\end{aligned} \tag{B.2}$$

Without loss of generality, we assume that $\alpha(t)$-parameter is real, and neglect the thermal excitation of microwave photons in the CPW-TLR at ultra-low temperature (e.g., below 20mK). As a consequence, the p-th qubit can be independently addressed and described effectively by the Hamiltonian:

$$\hat{H}''_p = \frac{1}{2}\hbar(\triangle_{pd} + \frac{\hbar g_p^2}{\triangle_p})\hat{\sigma}_p^z + \hbar g_p\alpha(t)(\hat{\sigma}_p^- + \hat{\sigma}_p^+), \tag{B.3}$$

with $\triangle_p = |\omega_p - \omega_r|$. The corresponding time evolution operator reads:

$$U_p(t) = \exp\left(-\frac{\mathrm{i}}{\hbar}\hat{H}_p'' t\right) = \begin{pmatrix} \cos\left[\frac{A(t)}{2}\right] & -i\sin\left[\frac{A(t)}{2}\right] \\ -i\sin\left[\frac{A(t)}{2}\right] & \cos\left[\frac{A(t)}{2}\right] \end{pmatrix}, \tag{B.4}$$

with $A(t) = 2\int_0^t g\alpha(t')dt'$. This is Equation (16).

References

[1] Coccia M 2022 Disruptive innovations in quantum technologies for social change *J. Econ. Bib.* **9** 21

[2] Arute F *et al* 2019 Quantum supremacy using a programmable superconducting processor *Nature* **574** 505

[3] Zhong H S *et al* 2020 Quantum computational advantage using photons *Science* **370** 1460

[4] Barends R *et al* 2016 Digitized adiabatic quantum computing with a superconducting circuit *Nature* **534** 222

[5] Inagaki T, Inaba K, Hamerly R, Inoue K, Yamamoto Y and Takesue H 2016 Large-scale Ising spin network based on degenerate optical parametric oscillators *Nat. Photonics* **10** 415

[6] Mcmahon P L *et al* 2016 A fully programmable 100-spin coherent Ising machine with all-to-all connections *Science* **354** 614

[7] Martinis J M, Devoret M H and J Clarke 2020 Quantum Josephson junction circuits and the dawn of artificial atoms *Nat. Phys.* **16** 234

[8] Criac J I and Zoller P 1995 Quantum computations with cold trapped ions *Phys. Rev. Lett.* **74** 4091

[9] Monroe C, Meekhof D M, King B E, Itano W M and Wineland D J 1995 Demonstration of a fundamental quantum logic gate *Phys. Rev. Lett.* **75** 4714

[10] Schmidt-Kaler F *et al* 2003 Realization of the Cirac-Zoller controlled-NOT quantum gate *Nature* **422** 408

[11] Sackett C A *et al* 2000 Experimental entanglement of four particles *Nature* **404** 256

[12] Häffner H *et al* 2005 Scalable multiparticle entanglement of trapped ions *Nature* **438** 643

[13] Matthiesen C, Yu Q, Guo J, Alonso A M and Häffner H 2021 Trapping electrons in a room-temperature microwave paul trap *Phys. Rev.* X **11** 011019

[14] Yu Q, Alonso A M, Caminiti J, Beck K M, Sutherland R T, Leibfried D, Rodrigurz K J, Dhital M, Hemmerling B and Häffner H 2022 Feasibility study of quantum computing using trapped electrons *Phys. Rev.* A **105** 022420

[15] Knill E, Laflamme R and Milburn G J 2001 A scheme for efficient quantum computation with linear optics *Nature* **409** 46

[16] Kok P, Munro W J, Nemoto K, Ralph T C, Dowling J P and Milburn G J 2007 Linear optical quantum computing with photonic qubits *Rev. Mod. Phys.* **79** 135

[17] Zajac D M, Hazard T M, Mi X, Nielsen E and Petta J R 2016 Scalable gate architecture for a one-dimensional array of semiconductor spin qubits *Phys. Rev. Appl.* **6** 054013

[18] Jones C, Fogarty M A, Morello A, Gyure M F, Dzurak A S and Ladd T D 2018 Logical qubit in a linear array of semiconductor quantum dots *Phys. Rev.* X **8** 021058

[19] Vajner D A, Rickert L, Gao T, Kaymazlar K and Heindel T 2022 Quantum communication using semiconductor quantum dots *Adv. Quantum Technol.* **5** 2100116

[20] Platzman P M and Dykman M I 1999 Quantum computing with electrons floating on liquid Helium *Science* **284** 1967

[21] Schuster D I, Fragner A, Dykman M I, Lyon S A and Schoelkopf R J 2010 Proposal for manipulating and detecting spin and orbital states of trapped electrons on Helium using cavity quantum electrodynamics *Phys. Rev. Lett.* **105** 040503

[22] Lyon S A 2006 Spin-based quantum computing using electrons on liquid Helium *Phys. Rev.* A **74** 052338

[23] Dykman M I, Platzman P M and P Seddighrad 2003 Qubits with electrons on liquid Helium *Phys. Rev.* B **67** 155402

[24] Koolstra G, Yang G and Schuster D I 2019 Coupling a single electron on superfluid Helium to a superconducting resonator, *Nat. Commun.* **10** 5323
[25] Zhang M, Jia H Y, Huang J S and Wei L F 2010 Strong couplings between artificial atoms and terahertz cavities *Opt. Lett.* **35** 1686
[26] Zhang M, Jia H Y and Wei L F 2009 Jaynes-Cummings models with trapped electrons on liquid helium *Phys. Rev.* A **80** 055801
[27] Kawakami E, Elarabi A and Konstantinov D 2021 Relaxation of the excited rydberg states of surface electrons on liquid Helium *Phys. Rev. Lett.* **126** 106802
[28] Zou S and Konstantinov D 2022 Image-charge detection of the Rydberg transition of electrons on superfluid helium confined in a microchannel structure *New J. Phys.* **24** 103026
[29] Grimes C C and Adams G 1979 Evidence for a liquid-to-crystal phase transition in a classical, two-dimensional sheet of electrons *Phys. Rev. Lett.* **42** 12
[30] Grimes C C, Brown T R, Burns M L and Zipfel C L 1976 Spectroscopy of electrons in image-potential-induced surface states outside liquid Helium *Phys. Rev.* B **13** 140
[31] Fragner A A 2013 Circuit quantum electrodynamics with electrons on Helium *PhD Theses* Yale University
[32] Woolf M A and Rayfield G W 1965 Energy of negative ions in liquid Helium by photoelectric injection *Phys. Rev. Lett.* **15** 235
[33] Grimes C C 1979 Cyclotron resonance in a two-dimensional electron gas on helium surfaces *J. Magn. Magn. Mater.* **11** 32
[34] Armbrust N, Güdde J and Höfer U 2016 Spectroscopy and dynamics of a two-dimensional electron gas on ultrathin Helium films on Cu(111) *Phys. Rev. Lett.* **116** 256801
[35] Glasson P, Dotsenko V, Fozooni P, Lea M J, Bailey W and Papageorgiou G 2001 Observation of dynamical ordering in a confined Wigner crystal *Phys. Rev. Lett.* **87** 17
[36] Gao F *et al* 2020 Site-controlled uniform Ge/Si hut wires with electrically tunable spin-orbit coupling *Adv. Mater.* **32** 1906523
[37] Cridland A, Lacy J H, Pinder J and Verdú J 2016 Single microwave photon detection with a trapped electron *Photonics* **3** 59
[38] Blais A, Grimsmo A L, Girvin S M and Wallraff A 2021 Circuit quantum electrodynamics *Rev. Mod. Phys.* **93** 025005
[39] Göppl M, Fragner A, Baur M, Bianchetti R, Filipp S, Fink J M, Leek P J, Puebla G, Steffen L and Wallraff A 2008 Coplanar waveguide resonators for circuit quantum electrodynamics *J. Appl. Phys.* **104** 113904
[40] Yang G 2020 Circuit quantum electrodynamics with electrons on Helium *PhD Thesis* University of Chicago
[41] Yang G, Fragner A, Koolstra G, Ocola L, Czaplewski D A, Schoelkopf R J and Schuster D I 2016 Coupling an ensemble of electrons on superfluid Helium to a superconducting circuit *Phys. Rev.* X **6** 011031
[42] Blais A, Huang R S, Wallraff A, Girvin S M and Schoelkopf R J 2004 Cavity quantum electrodynamics for superconducting electrical circuits: An architecture for quantum computation *Phys. Rev.* A **69** 062320
[43] Blais A, Gambetta J, Wallraff A, Schuster D I, Girvin S M, Devoret M H and Schoelkopf R J 2007 Quantum-information processing with circuit quantum electrodynamics *Phys. Rev.* A **75** 032329
[44] Kawakami E, Elarabi A and Konstantinov D 2019 Image-charge detection of the Rydberg states of surface electrons on liquid Helium *Phys. Rev. Lett.* **123** 086801
[45] Zhou X J *et al* 2022 Single electrons on solid neon as a solid-state qubit platform *Nature* **605** 46
[46] Raha M, Chen S T, Phenicie C M, Ourari S, Dibos A M and Thompson J D 2020 Optical quantum nondemolition measurement of a single rare earth ion qubit *Nat. Commun.* **11** 1605
[47] Gómez-León Á, Luis F and Zueco D 2022 Dispersive readout of molecular spin qudits *Phys. Rev. Applied* **17** 064030
[48] Schuster D I *et al* 2007 Resolving photon number states in a superconducting circuit *nature* **445** 515
[49] Li P Z and Loock P V 2023 Memoryless quantum repeaters based on cavity-QED and coherent states *Adv. Quantum Technol.* **6** 2200151
[50] Walls D F and Milburn G J 1995 *Quantum Optics* (Springer, Berlin, Heidelberg) p 121
[51] Guo W J, Wang Y and Wei L F 2016 Controllable photon bunching by atomic superpositions in a driven cavity *Phys. Rev.* A **93** 043809

[52] Huang J S, Oh C H and L F Wei 2011 Testing tripartite Mermin inequalities by spectral joint measurements of qubits *Phys. Rev.* A **83** 062108

[53] Huang J S, Wei L F and Oh C H 2011 High-efficiency tomographic reconstruction of quantum states by quantum nondemolition measurements *Phys. Rev.* A **83** 032110

[54] Yuan H, Wei L F, Huang J S and Vedral V 2012 Quantum nonlocality test by spectral joint measurements of qubits in driven cavity *Europhys. Lett.* **100** 10007

[55] Jeffrey E *et al* 2014 Fast accurate state measurement in superconducting qubits *Phys. Rev. Lett.* **112** 190504

[56] He Q, Ouyang P, Gao H, He S, Li Y, Wang Y, Dai X, Wang Y and Wei L F 2022 Low-loss superconducting aluminum microwave coplanar waveguide resonators on sapphires for the qubit readouts *Supercond. Sci. Technol.* **35** 065017